

VOLUMETRIC IMAGE REGISTRATION METHODS BASED ON SOLVING THE MONGE-AMPÈRE EQUATION

M. M. SULMAN*, JF WILLIAMS†, M. F. BEG† R. D. RUSSELL†

Abstract. Two new approaches for solving the image registration problem are investigated. Both use optimal warping and an elastic registration approach and are based on solving the Monge-Ampère equation fundamental to the Monge-Kantorovich theory for optimal mass transport. The key idea of the first method is to find a steady state solution to the parabolic Monge-Ampère equation. The second approach uses a fluid mechanics formulation of the optimal mass transfer problem. Several examples are given to demonstrate the performance of the methods.

1. Introduction. Volumetric image registration is the process in which a geometric transformation between two images, one of which is called the template, and the other the target, is found such that features in one image are mapped to the homologous features in the other. For matching anatomical images, these transformations are ideally desired to be bijective (one-to-one, and onto) so that neighborhood structure is maintained, and continuous with continuous inverse, so that tears are not created by the transformation. Also, geometric transformations act purely on the background domain and the image intensity values are merely labels, or material, that is transported by the transformation from one location to another within the domain. The quality of the registration is measured by a data-attachment term which captures how well the transformed template image matches the target image, and from all the different transformations that could yield the same quality of registration, an optimal one is determined by computing an index of the efficacy of the transformation, such as smoothness. These two terms may be merged together into a single cost function, with optimization used to find a candidate optimal transformation.

The existing methods for computing volumetric registration can be classified based on how they model the data-attachment term, and the transformation model itself. The data-attachment term can be based on specification of correspondences (often prescribed on a small set of landmarks, curves or surfaces) [?, ?, ?, ?, ?, ?] or some index of similarity on the image intensity values itself ranging from the usual L^2 norm of the error, the mutual information cost suited for cross-modality matching, correlation, to a rich set of attribute vectors [?, ?, ?, ?, ?, ?, ?]. The transformation model can be low dimensional (affine), or high dimensional models using displacement vector fields (elastic methods) or time-dependent vector fields (the so-called "fluid" or large deformation diffeomorphism based methods) [?, ?, ?, ?, ?, ?, ?, ?]. Excellent overview and discussion of these methods can be found in [?, ?, ?].

Volumetric registration has also been formulated as an optimal mass transport problem. Mathematical models of transporting material from one location to another at minimal cost were extensively studied by Monge in 1781 and by Kantorovich in 1942, and are known as the Monge-Kantorovich theory of optimal mass transport. Haker et al. [?] proposed an elastic registration method which is solved via an optimal warping based on deriving a partial differential equation to minimize the L^2 Kantorovich-Wassertein distance under a mass preservation constraint. In this

*DEPARTMENT OF MATHEMATICS, SIMON FRASER UNIVERSITY, BURNABY, BRITISH COLUMBIA, V5A 1S6 CANADA.

†SCHOOL OF ENGINEERING SCIENCE, SIMON FRASER UNIVERSITY, BURNABY, BRITISH COLUMBIA, V5A 1S6 CANADA.

paper we present two new approaches to the optimal warping solution of the elastic registration problem which are based on solving the Monge–Ampère equation (MAE) found in the Monge–Kantorovich theory of the optimal mass transport problem. Our first approach for registration is based on finding a steady state solution of a suitable time dependent parabolic Monge Ampère equation (PMAE). This steady state solution is the solution of the original Monge–Ampère equation derived in the Monge–Kantorovich theory. The second approach is based on solving the optimal mass transport problem in a fluid dynamics framework (see [?, ?]), where we treat the image intensities as densities. The first formulation is solved via standard finite differences and the second using the saddle-point description of Benamou and Brenier [?]. Our optimal solution of the L^2 Monge–Kantorovich problem is hence obtained as the gradient of the steady-state solution of a parabolic partial differential equation starting from an identity mapping. In [?, ?, ?], the optimal mapping is found as a gradient flow that requires constructing an initial map found by solving a family of one-dimensional mass transport problems.

2. The Optimal Mass Transport Problem. We first briefly review the original Monge–Kantorovich optimal transport problem (MKP), see [?, ?, ?] for more details on the subject. Let the domains Ω_0 and Ω_1 be given as subsets of \mathbb{R}^d and scalar functions $\rho_0 : \Omega_0 \rightarrow \mathbb{R}$ and $\rho_1 : \Omega_1 \rightarrow \mathbb{R}$ be defined on the domains Ω_0 and Ω_1 , respectively, such that they are both bounded and positive definite. These functions model the density of material, and the integral density over a given volume is the mass of material in that volume. It is assumed that the total mass of the material is normalized to one,

$$\int_{\mathbb{R}^d} \rho_0(x) dx = \int_{\mathbb{R}^d} \rho_1(x) dx = 1. \quad (2.1)$$

The transport problem seeks to find a mapping $\phi : \Omega_0 \rightarrow \Omega_1$ that moves the point $x \in \Omega_0$ to location $\phi(x) \in \Omega_1$ with displacement $u(x) = \phi(x) - x$ such that the density of material ρ_0 in domain Ω_0 is transferred to become the density ρ_1 given in the domain Ω_1 . This is the data matching constraint of the problem. Mathematically, the mass of material in any bounded subset $\Omega \subseteq \Omega_1$ must then equal the mass of material coming from the pre-image $\phi^{-1}(\Omega) \subseteq \Omega_0$ i.e.

$$\int_{\phi^{-1}(\Omega)} \rho_0(x) dx = \int_{\Omega} \rho_1(x) dx \quad (2.2)$$

for all bounded subsets Ω of Ω_1 .

If $\phi(x)$ is a smooth one-to-one map then by a change of variables, (2.2) leads to the Jacobian equation

$$\rho_1(\phi(x)) |D\phi(x)| = \rho_0(x), \quad (2.3)$$

where $|D\phi(x)|$ is the determinant of the Jacobian that describes the distortions of the local area element induced by the map ϕ . The solution to (2.3) is not unique as it is only one equation involving d unknowns. We need an additional closure condition to determine uniqueness. For our closure condition we seek the solution which minimizes the cost functional

$$C(\phi) = \int_{\Omega_0} |\phi(x) - x|^p \rho_0(x) dx. \quad (2.4)$$

The same task, framed in terms of finding the optimal displacement vector fields u , takes the form of optimizing

$$C(u) = \int_{\Omega_0} |u(x)|^p \rho_0(x) dx. \quad (2.5)$$

For $p = 1$, one can interpret this as being an overall measure of effort required or *work done* to transform one pile of mass to another. The amount of work required to transfer one mass density to another can also be interpreted as a measure of a distance between them; if the piles of mass are *similar*, then the amount of work needed to transfer one to the other will be correspondingly small. This is an intuitive motivation for the L^p Kantorovich (or Wasserstein) distance between the given density functions ρ_0, ρ_1 that is defined as

$$d(\rho_0, \rho_1) = \inf_{\phi} \left(\int_{\Omega_0} |\phi(x) - x|^p \rho_0(x) dx \right)^{\frac{1}{p}}. \quad (2.6)$$

In terms of displacements, we can write the above distance as equivalently being

$$d(\rho_0, \rho_1) = \inf_u \left(\int_{\Omega_0} |u(x)|^p \rho_0(x) dx \right)^{\frac{1}{p}}. \quad (2.7)$$

For $p = 2$, both of the cost functions (2.4) and (2.5) are essentially a form of Euclidean distance weighted by the mass being transferred. A one-to-one mapping $y = \phi(x)$ that satisfies (2.3) and minimizes the cost (2.4) (or equivalently (2.5)) is then called an *optimal solution* to the L^p Monge-Kantorovich transport problem.

In this paper we only concern ourselves with the L^2 costs (where $p = 2$) because of its mathematical simplicity and because of its links to existing registration methods. For this case, Brenier and Benamou [?] show a direct link between the L^2 MKP and fluid dynamics. As well, the cost (2.4) for $p = 2$ has known desirable mathematical properties and has been used extensively in diverse fields of applications, such as mathematical finance, functional analysis, atmospheric sciences, shape recognition in image processing, computer vision, and signal processing — see the book [?] and the references therein.

In this paper, we use an optimal transportation framework to perform image registration. While the optimal transport problem was motivated by problems in finding good ways to transport material piles from one location to another, the same formulation can also be used for finding a mapping between two given gray-scale images. In this case, the density functions are replaced by the image intensity functions (also bounded and positive). The L^2 Kantorovich distance is a quantitative information measure for comparing two different density functions (intensity functions for the case of images). This makes the approach useful for image registration, particularly for medical images.

Here, we are seeking maps which deform one image to another while minimizing the cost of moving the pixels. Because pixels have, unlike sand, no intrinsic weight, this approach may at first seem naive. However, the minimizer of the transport problem has many regularity properties which make it well suited for this mapping problem. Indeed, using the cost (2.4) for finding the optimal solution leads to a very similar form to the fluid image deformation method of Beg et al. [?] and to that of Haker et al. (see [?], [?], [?] and [?]). However, we use a different and simpler approach to solve for the optimal mapping.

The basic theoretical result for the L^2 MKP (see [?]) which motivates what follows is in [?]. Brenier proves that there is a unique optimal solution $y = \hat{\phi}(x)$ characterized as the unique mapping which transfers ρ_0 to ρ_1 , and that it can be written as the gradient of a convex potential function $\Psi(x)$, i.e.,

$$\hat{\phi}(x) = \nabla\Psi(x). \quad (2.8)$$

Substituting (2.8) into (2.3) shows that Ψ is a solution of the Monge-Ampère equation (MAE)

$$|D^2\Psi(x)| \rho_1(\nabla\Psi(x)) = \rho_0(x), \quad (2.9)$$

where $D^2\Psi$ denotes the Hessian matrix of Ψ . The solution of the L^2 Monge-Kantorovich mass transfer problem thus reduces to solving the Monge-Ampère equation (2.9). The resulting map is one-to-one, since it is the gradient of a convex function. Moreover, $\Psi(x)$ is unique up to affine transformations which are generally specified by the boundary conditions. Nevertheless, solving (2.9) can itself be very challenging.

It is helpful to observe that the solution form (2.8) implies that the mapping is a Legendre transformation. Such mappings have the property that they are invertible and that their inverses are also Legendre transformations with a special structural relation between them [?].

3. The PMAE Approach to Solve the MKP. In this Section we present our alternative approach to solve for the optimal mapping in 2 or 3-dimensional space. The approach involves finding a solution to (2.9) as a steady state solution of the parabolic Monge-Ampère equation (PMAE)

$$\frac{\partial\Psi}{\partial t} = \log\left(\frac{|D^2\Psi|\rho_1(\nabla\Psi)}{\rho_0(x)}\right). \quad (3.1)$$

We integrate (3.1) in conjunction with the initial and Neumann boundary conditions

$$\Psi(x, 0) = \Psi_0(x) = \frac{1}{2}x \cdot x^T. \quad (3.2)$$

and

$$\nabla\Psi \cdot \mathbf{n} = x \cdot \mathbf{n}, \quad \text{on } \partial\Omega, \quad (3.3)$$

where \mathbf{n} denotes the unit outward normal vector field to $\partial\Omega$. These boundary conditions ensure that the boundaries of the images map to each other. The choice of the boundary condition 3.3 is appropriate since in image registration it is always possible to adjust the two images such that the active area of the deformation is away from the boundary.

A number of theoretical issues, such as convergence, stability and regularity, arise when solving the nonlinear partial differential equations to steady state. It is known that the elliptic Monge-Ampère equation (2.9) has a unique solution and that its regularity is determined by the regularity of the densities and the domain. Caffarelli [?,?] has shown that if Ω_1 is convex and $\rho_0, 1/\rho_1$ are bounded, then (2.9) has solution such that (i) the mapping is one-to-one as Ψ is strictly convex; (ii) the mapping is continuous as $\Psi \in C^{1,\beta}$ for some $\beta > 0$; (iii) if ρ_0 and ρ_1 are continuous then the Jacobian of the mapping is in L^p for every p and (iv) if ρ_0 and ρ_1 are in C^q then $\Psi \in C^p$ for all $p < q$.

Caffarelli’s results provide restrictions on the regularity of the mapping when the densities are discontinuous and where there are corners in the domains. It is important to note that these issues are real and not merely technical. In Section 5 we construct an exact mapping for a pair of discontinuous densities and see that the mapping is continuous while its gradient is not. Calculations presented in [?] show that there is a compatibility condition for smooth mappings between domains with corners. This condition is trivially satisfied when the normal derivative of both densities is zero on faces, which generally be ensured for the image registration problem (possibly by adjusting the domains). Hence, in practice the continuity of the mapping is guaranteed, and regularity is determined by the regularity of the image, for example mappings of binary images will have piecewise discontinuous gradients.

There are additional technical details to consider when solving the evolutionary equation (3.1). Convergence to this stationary solution is proved by standard sub- and super-solution arguments — e.g., see Budd and Williams [?], who solve parabolic Monge–Ampère equations of a similar form to (3.1) in the context of developing moving mesh methods to solve PDEs, and they show as well that there is an exponential convergence in a neighborhood of the stationary solution [?]. Recently, Sulman [?] describes the global existence, uniqueness and convergence of the solution of the initial boundary value problem (3.1), (3.3), (3.2) to the unique solution of the Monge–Ampère equation (2.9) under suitable regularity and structure on Ω , ρ_0 , ρ_1 and f . Thus, the evolution of (3.1) converges to the solution of (2.9).

In order to obtain an approximate solution to the original MAE (2.9) we solve (3.1) with suitable temporal initial and spatial boundary conditions to obtain the limiting solution Ψ^∞ as $t \rightarrow \infty$. The optimal transformation $\hat{\phi}$ is then obtained by taking the gradient of Ψ^∞ , i.e., $\hat{\phi} = \nabla\Psi^\infty$. The corresponding flow $\phi(x, t)$ for the image warping (deformation) is defined as

$$\phi(x, t) = x + t(\nabla\Psi^\infty(x) - x), \quad x \in \Omega_0, \quad 0 \leq t \leq 1. \quad (3.4)$$

The formula (3.4) is a direct consequence of Benamou and Brenier [?] fluid dynamic formulation of the L^2 Monge–Kantorovich formulation. The formula (3.4) shows that at time $t = 0$, ϕ is the identity map and at $t = 1$, it is the optimal solution of the L^2 Monge–Kantorovich problem. Thus, the formula (3.4) can be used to define continuous warping map ϕ between the initial density ρ_0 and the final density ρ_1 . The interpolation (3.4) generates the density and velocity which minimize the related functional (cf. 4.3 below), although other interpolation methods could also be used, such as that in [?].

We have focused on constructing a time-like formulation (3.1) to solve (2.9) in order to compare it to other time-like methods, permit solving problems with dynamic densities, and enable use of the computed solution as an interpolant. Work on developing a numerical method which alternatively solves the elliptic problem (2.9) directly is currently underway as well.

3.1. Computational Details. In this section we discuss some of the numerical details of solving (3.1) for the solution Ψ and its gradient to find the optimal transformation. For the examples presented in Section 5, we use a standard centered finite difference scheme for the spatial discretization of (3.1) and an explicit scheme such as forward Euler or a higher-order Runge–Kutta scheme in time. The simplest algorithm to compute Ψ is the following:

1. Given Ψ^n
2. Compute the spatial derivatives $D^2\Psi^n$ and $\nabla\Psi^n$

3. Interpolate ρ_1 onto $\nabla\Psi^n$
4. Set

$$F^n = \log\left(\frac{|D^2\Psi|\rho_1(\nabla\Psi(x))}{\rho_0(x)}\right)$$

5. Update Ψ^n : $\Psi^{n+1} = \Psi^n + \Delta t F^n$
6. If $\|\nabla F^n\| < \tau$ STOP, else set $n = n + 1$ and go to 2.

We iterate as $t \rightarrow \infty$, and in practice stop when the steady state map is approximated sufficiently well, viz., when $\|\nabla(\Psi^{n+1} - \Psi^n)\|_{L^2} \leq \Delta t \tau$, for some specified tolerance τ and time-step Δt . Using Δt in the stopping criterion guarantees that the time derivatives of the map itself is small. Also, while the integrals of the original image intensities are normalized to unity, numerical error can perturb this, leading to a solution for the potential Ψ which can slowly translate uniformly in time with no impact on the mapping $\phi = \nabla\Psi$.

3.2. Boundary and Initial conditions. The method is applied to 2D or 3D images defined on a unit square or unit cubic domain, respectively, using the Neumann conditions

$$\frac{\partial\Psi}{\partial x_i} = 0, \quad \text{on } x_i = 0, \quad \frac{\partial\Psi}{\partial x_i} = 1, \quad \text{on } x_i = 1, \quad i = 1, 2, \text{ or } 3. \quad (3.5)$$

We start with a uniform mesh, taking $\Psi(x, 0) = \frac{1}{2}x^T x$. Using this and equation (3.5), the method is simple and efficient, with no need to compute an initial mapping.

3.3. The Stopping Criterion. We derive the stopping criterion based on the observation that the gradient of the solution of the Monge-Ampère equation (2.9) is unique. Therefore, if the steady-state solution of (3.1) exists then it is unique up to a constant, i.e., $\nabla\Psi^\infty$, is the unique minimizer of the cost functional (2.4), for $p = 2$. This concludes that the functional

$$C(\Psi(x, t)) = \int_{\Omega_c} |\nabla\Psi(x, t) - x|^2 \rho_0(x) dx \quad (3.6)$$

is decreasing in time and its minimum is achieved as $t \rightarrow \infty$. Thus, $\|\nabla\Psi(x, t) - x\|_2$, $t > 0$, changes slowly, with respect to x , close to the steady-state solution. This means that

$$\nabla\Psi_t \rightarrow 0 \text{ as } t \rightarrow \infty, \quad (3.7)$$

where Ψ_t is the partial derivative of $\Psi(x, t)$ with respect to t . Therefore, we use the following convergence criterion

$$\text{res}^n = \|\nabla\Psi_t^n\|_2 = \left(\int_{\Omega_c} |\nabla\Psi_t(t, t^n)|^2 dx\right)^{\frac{1}{2}} \leq \tau \quad (3.8)$$

where τ is the user defined tolerance.

4. Fluid Dynamics Formulation of the MKP. The Monge-Ampère equation (2.9) is fully nonlinear and raises many numerical challenges. In order to avoid solving equation (2.9) directly, Benamou and Brenier introduce a fluid dynamics framework for the Monge-Kantorovich problem in [?]. To this end, they fix a time interval $[0, T]$ which for simplicity we take to be $[0, 1]$, and consider all possible sufficiently smooth

time-dependent density and velocity fields $\rho_t(x) > 0$, $v_t(x) \in \mathbb{R}^d$ which satisfy the continuity equation

$$\frac{\partial \rho_t}{\partial t} + \nabla \cdot (\rho_t v_t) = 0 \quad (4.1)$$

for $0 \leq t \leq 1$, $x \in \mathbb{R}^d$ and the initial and final conditions

$$\rho_0(\cdot) = \rho_0, \quad \rho_1(\cdot) = \rho_1. \quad (4.2)$$

Here the ρ_t notation denotes a time-dependent flow of density functions that is to be computed as part of the solution.

That is, the velocity fields transfer the initial density ρ_0 to the final density ρ_1 . If we were to follow the motion of a point $x \in \Omega_0$, then it now follows a time-dependent trajectory $\phi_t(x)$, $t \in [0, 1]$ and the final position of this point in the destination is $\phi_1(x)$. Thus, the overall displacement of the point needed to reach its target location is $u(x) = \phi_1(x) - x$.

The relationship between the Monge-Kantorovich problem and fluid dynamics was established by Benamou and Brenier in [?] where they proved that the square of the L^2 Kantorovich distance is equal to the infimum of the cost functional

$$C(\rho_t, v_t) = \int_0^1 \int_{\mathbb{R}^d} \rho_t(x) |v_t(x)|^2 dx dt, \quad (4.3)$$

where the density and velocity fields (ρ_t, v_t) satisfy the conditions (4.1) and (4.2).

This shows that the L^2 Monge-Kantorovich problem may be reformulated as finding the velocity vector field $v_t(x)$ by minimizing the functional (4.3) under the constraints (4.1) and (4.2), i.e., we find $(\hat{\rho}, \hat{v})$ which solve the minimization problem

$$C(\hat{\rho}, \hat{v}_t) = \inf_{(\rho, v_t)} \int_0^1 \int_{\mathbb{R}^d} \rho_t(x) |v_t(x)|^2 dx dt. \quad (4.4)$$

The fluid dynamics formulation of the Monge-Kantorovich problem (FDMKP) provides a natural time interpolant $\rho_t(x)$ from the data ρ_0 to ρ_1 and a velocity field $v_t(x)$ which transports ρ_0 to ρ_1 . This is very useful for an elastic image registration method.

Beg et al. [?] use a similar energy functional to (4.3) to derive a method of image registration based on solving the minimization problem

$$\hat{v}_t = \underset{v_t}{\operatorname{argmin}} \left(\int_0^1 \|v_t\|_V^2 dt + \frac{1}{\sigma^2} \|\rho_0 \circ \phi_1^{-1} - \rho_1\|_{L^2}^2 \right), \quad (4.5)$$

whose solution over the space V of all smooth velocity vector fields gives the optimal change of coordinates ϕ_1 between ρ_0 and ρ_1 to be matched. The norm $\|v\|_V$ is an appropriate Sobolev norm on V .

Note that the minimization problem (4.5) is formally very similar to that of (4.4). In fact, the second term in (4.5) simply enforces that the matching of the images be exact at $t = 1$ as the relaxation parameter $\sigma^2 \rightarrow 0$, whereas the temporal boundary conditions are taken as constraints in the fluid dynamics formulation. In the case where $\|v_t\|_V$ is the L^2 norm weighted by the transported density, we exactly recover (4.4). Mathematically, this weight is the primary difference between our approach and that in [?].

We solve the minimization problem (4.5) using the numerical method of Benamou and Brenier [?] derived for solving the equivalent saddle-point problem. In Section 5 this FDMKP method is applied to register images in 2 spatial dimensions (2D) for several examples. A drawback of this approach for 3D images is the need to solve the space-time Poisson equation in four dimensions which results in solving the minimization problem (4.4) under the constraints (4.1) and (4.2). This makes the method fairly complicated and costly, particularly for large size images.

5. Numerical Experiments. In this Section we present numerous examples to illustrate the properties of our new methods. The examples have been chosen to give the reader some insight into how the method works for both simple problems and more practical real world examples. For completeness we present calculations from using both the Fluid Dynamics formulation (FDKMP) and the parabolic Monge-Ampère equation (PMAE).

5.1. Examples. EXAMPLE 1 We begin with the simple problem of computing a mapping from one circle to another concentric one using the FDMKP method. For radially symmetric densities, the solution of the Monge-Ampère equation (2.9) can be found exactly by direct integration. Specifically, defining the polar co-ordinates

$$\xi = r \cos(\theta), \quad \eta = r \sin(\theta), \quad \xi, \eta \in \Omega_0,$$

the Monge-Ampère equation (2.9) simplifies to

$$\frac{1}{r} \Psi_r \Psi_{rr} = \frac{\rho_0(r)}{\rho_1(\Psi_r(r))} \quad (5.1)$$

where Ψ_r and Ψ_{rr} are the first and second derivatives with respect to the radial variable r . Here, the densities ρ_0 and ρ_1 are piecewise constant, so the right hand side of (5.1) is a constant, say a . Integrating (5.1) once gives

$$\Psi_r = \sqrt{a} \sqrt{r^2 + c}$$

where a is the ratio ρ_0/ρ_1 and c is the integration constant.

Note that our primary goal is to compute the optimal mapping that transfers ρ_0 to ρ_1 and not the potential $\Psi(r)$ in its entirety. Therefore, using (2.8) we obtain the optimal mapping in terms of Ψ_r as

$$x = \frac{\xi}{r} \Psi_r, \quad y = \frac{\eta}{r} \Psi_r.$$

The exact solution for the optimal transformation is shown in Figure 5.1.

We use the FDMKP method to compute the numerical solution for the optimal transformation. The numerical and the exact solutions are plotted in Figure 5.2 on a grid of size 33×33 . Notice that the numerical solution is smoother than the exact solution because of the regularization in the numerical discretization. The L^2 norm of the error in the numerical solution of for the optimal mapping is 0.0054. In this example, we use the optimal transformation to deform a circle (template image) to a smaller concentric circle (target image); therefore, the grid points are expected to be displaced radially towards the center of the circles. As expected, the displacement vector field (see Figure 5.2(a)) shows that the grid points have been moved radially

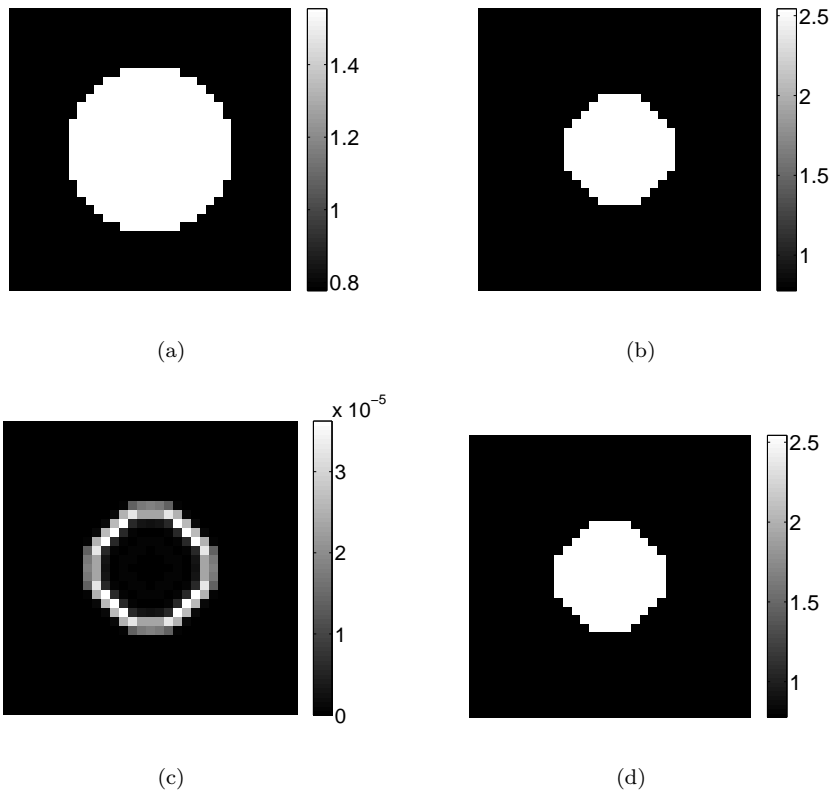


Fig. 5.1: Example 1. Registration of two concentric circles defined on a 33×33 grid. Shown here are (a) the template image, (b) reference image, (c) absolute error between the deformed template and the reference images, and (d) deformed template image obtained using the FDMKP method.

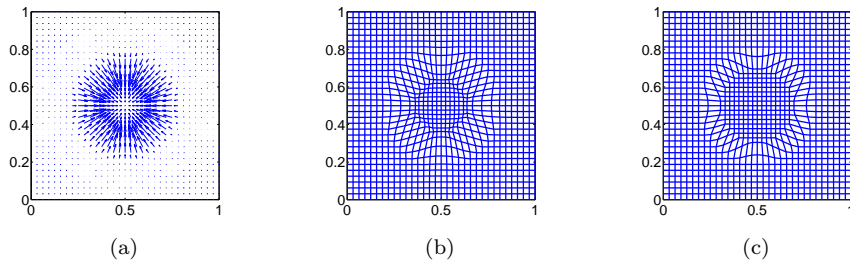


Fig. 5.2: Example 1. Image matching of two concentric circles. Shown here are (a) displacement vector field, (b) numerical solution for the optimal mapping computed using the FDMKP method on a grid of size 33×33 , and (c) exact solution for the optimal mapping. Observe that the numerical solution is smoother than the exact solution due to the regularization used in the numerical discretization.

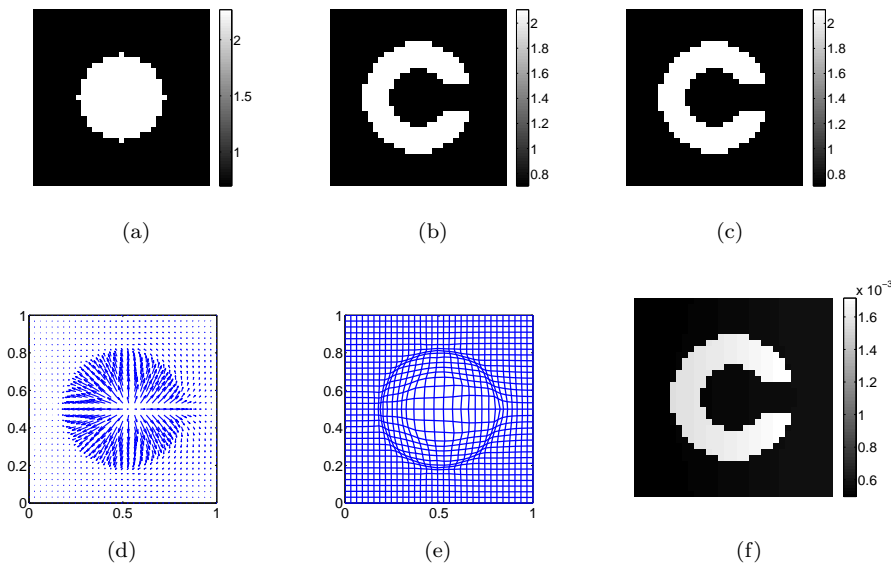


Fig. 5.3: Example 2. Registration of a circle (template) to a C-shape (target) using the PMKP method. Shown are the (a) template image, (b) reference image, (c) deformed template, (d) displacement vector field, (e) computed optimal transformation, and (f) absolute error between the deformed template and the target.

towards the center. In Figure 5.1(a), (b) and (d) we show the template, the target and the deformed images, respectively. We show the absolute error between the deformed image and the target image in Figure 5.1(c).

EXAMPLE 2 In this example we apply the PMAE method to perform a registration of a circle to a C-shape image as shown in Figure 5.3. The computed optimal matching mapping and the displacement vector field are given in Figure 5.3 (e) and (d), respectively. The displacement vector field shows that, as expected, the grid points have been moved radially towards the boundary of the circle. The deformed template image and the absolute error between the target and the deformed template are shown in Figure 5.3 (c) and (f).

EXAMPLE 3

Here the PMAE method is applied to register 3D images of two concentric spheres, from the outer sphere to the inner one. The densities are defined on a $32 \times 32 \times 32$ unit cube. In Figure 5.4 we show some slices of the 3D optimal matching mapping.

EXAMPLE 4 This is a practical example from medical imaging, where the FDMKP method is applied to register images. The template and target are cryosection images of the Macaque visual cortex (see Figure 5.5 (a) and (b)). The FDMKP method is applied to register the two images with 79×79 grid points. Figure 5.5 (d) and (e) presents the displacement vector field and the computed optimal matching transformation. In Figure 5.5 (c) and (f) we show the deformed template image and the absolute error between the target and the deformed images.

EXAMPLE 5

For this example, we apply the PMAE method to register 3D binary segmented images

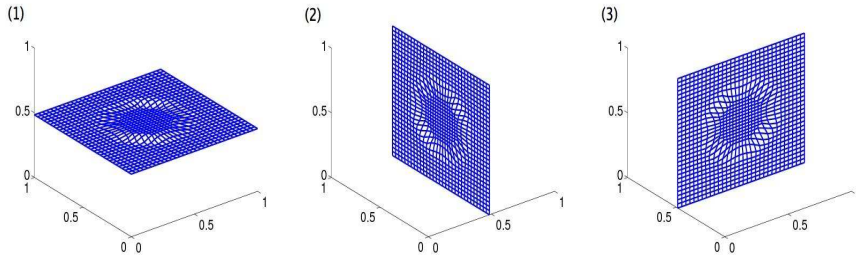


Fig. 5.4: Example 3. Registration of two spheres. Shown here are 3 slices of the 3D optimal transformation for the PMAE registration of one sphere onto another. The slice is number 16 in (1) the xy plane, (2) the xz plane, and (3) the yz plane.

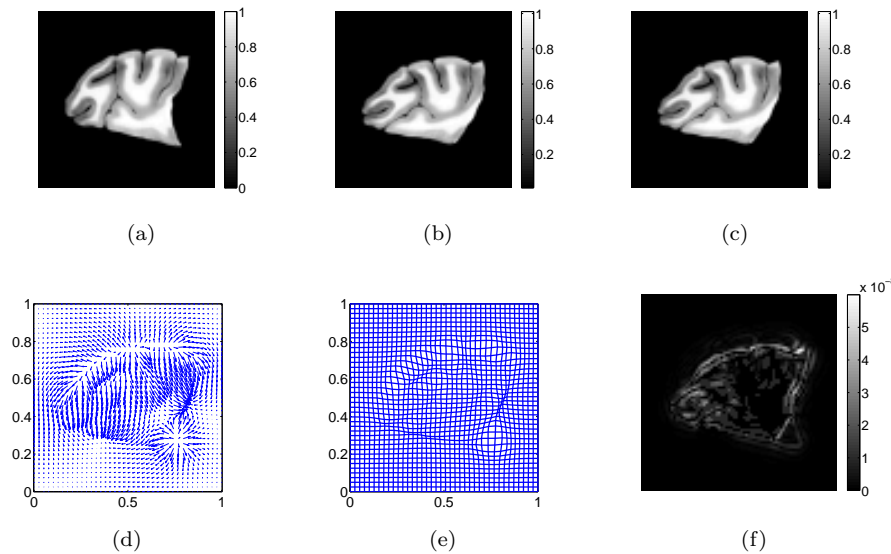


Fig. 5.5: Example 4. FDMKP registration of Macaque cortex. Shown are the (a) template image, (b) reference image, (c) deformed template, (d) displacement vector field, (e) computed optimal transformation, and (f) the absolute error between the deformed template and the target image.

of two canine hearts. The densities are defined on a $240 \times 240 \times 80$ grid. In Figure 5.6 we show the template, target, and deformed template images. Figure 5.7 shows some slices on the xy , yz , and xz planes for the computed optimal mapping.

EXAMPLE 6

The PMAE method is used to register a heart image (template) to six other heart images (targets). The size of each image is $128 \times 128 \times 128$. The results of the registration are shown in Figure 5.8. The template is shown on the first row. The first and the third columns show the six target images, with the second and fourth columns showing the corresponding six deformed images.

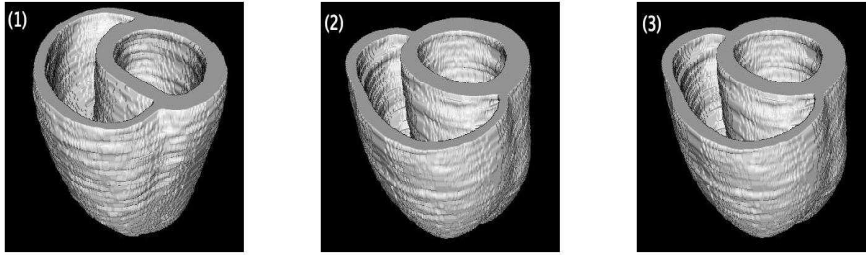


Fig. 5.6: Example 5. Registration of two 3D hearts of size $240 \times 240 \times 80$. Shown are the (1) heart template, (2) target, and (3) deformed template images obtained from solving the Monge-Ampère equation.

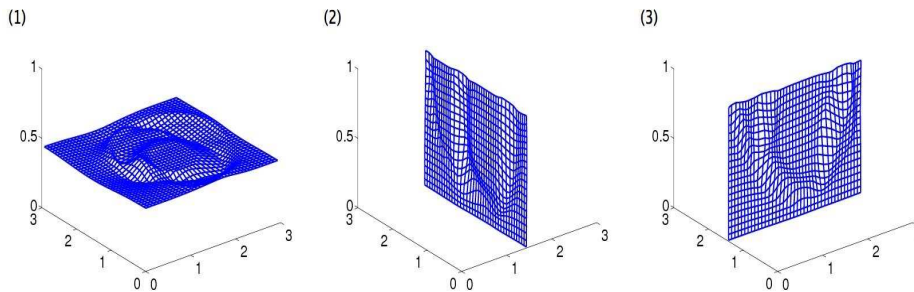


Fig. 5.7: Example 5. Registration of two 3D hearts. Shown are some slices of the optimal matching mapping on the (1) xy -plane, (2) yz -plane, and (3) xz -plane. To facilitate visualization, only a sector of each grid slice is plotted.

EXAMPLE 7

In this example the PMAE method is tested for the 3D binary segmentation images of the left and right hippocampus taken from brain MR images. The densities are defined on a $40 \times 64 \times 64$ grid. Figure 5.9, Figure 5.10 shows the results of registration of the (top) template to eight targets. Again, the first and third columns show the eight target images, and the second and fourth columns show the corresponding eight deformed images.

EXAMPLE 8

For this final example, the PMAE method is used for the registration of gray-scale images. Specifically, we apply the method for 2D slices taken from 3D brain MRI images from the IBSR data repository (publicly available from the Center for Morphometric Analysis, Massachusetts General Hospital). The size of each image is $80 \times 56 \times 80$. The results of the registration are shown in Figure 5.11, where the first row represents the registration of the midcoronal slices, the second row corresponds to the registration of the midsagittal slices, and the third row is for the registration of the midhorizontal slices. The first column shows the template image, the second column shows the target image and third column shows the deformed template.

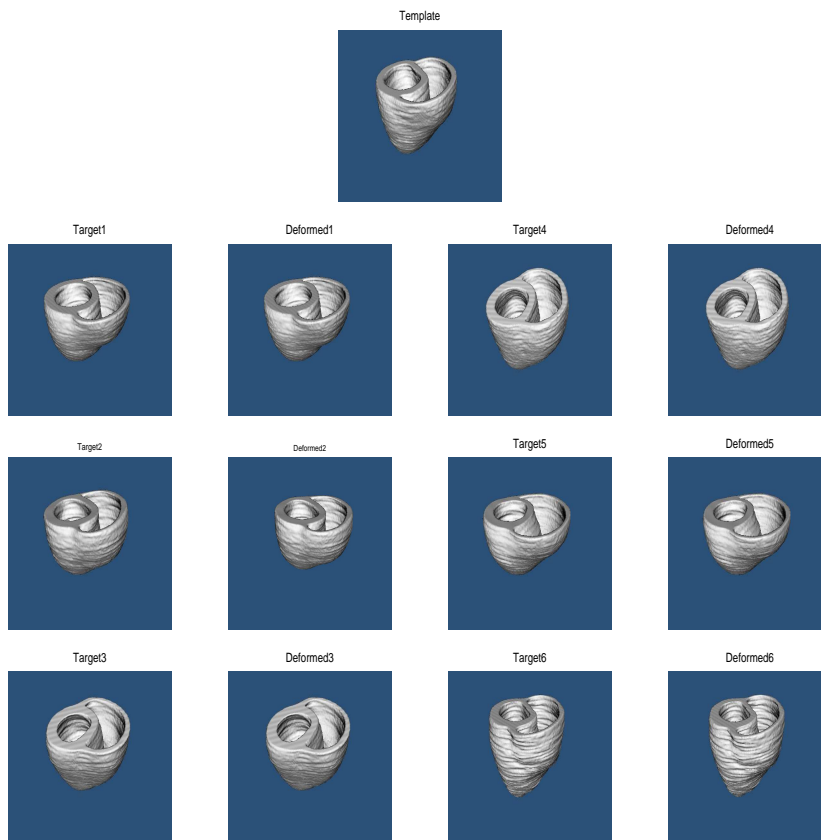


Fig. 5.8: Example 6. Registration of the a heart (template) to six other hearts (targets). The size of images is $128 \times 128 \times 128$. Template on the first row. The six pictures in the first and third columns show the targets. The corresponding eight deformed images are in the second and fourth columns.

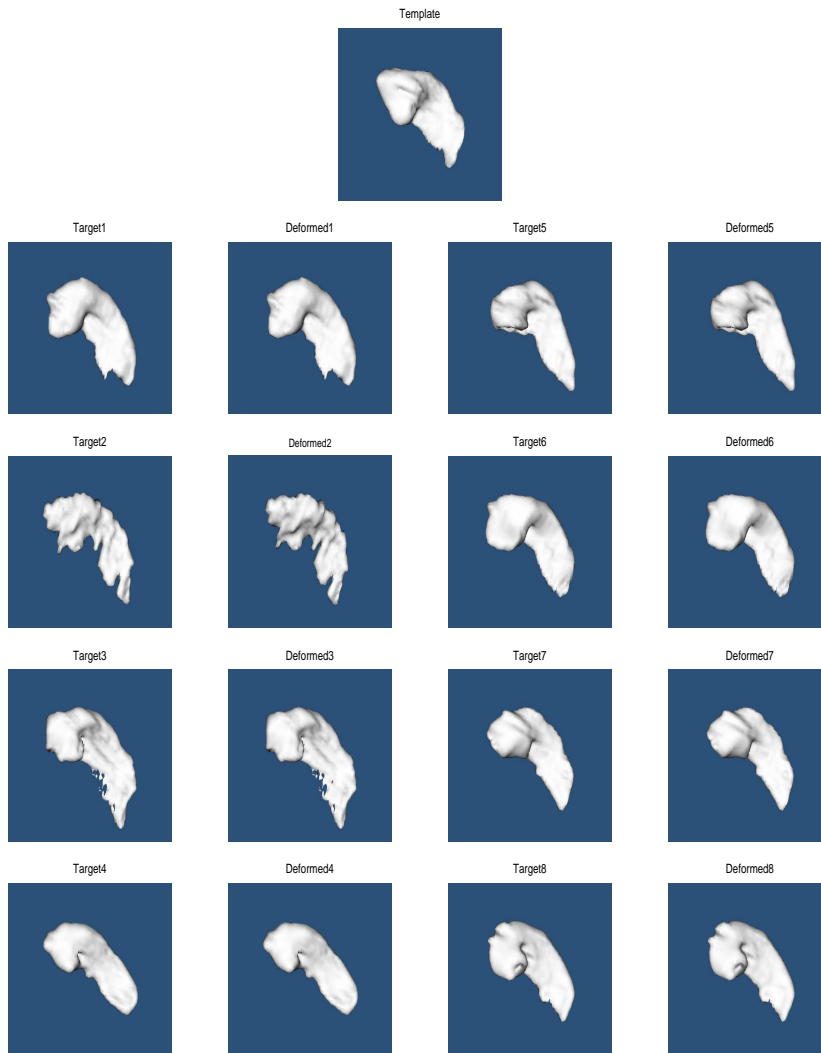


Fig. 5.9: Example 7. Registration of left hippocampus, the template shown in the first row, to eight other targets. The eight target images are shown in the first and third columns, and the corresponding eight deformed images are in the second and fourth columns.

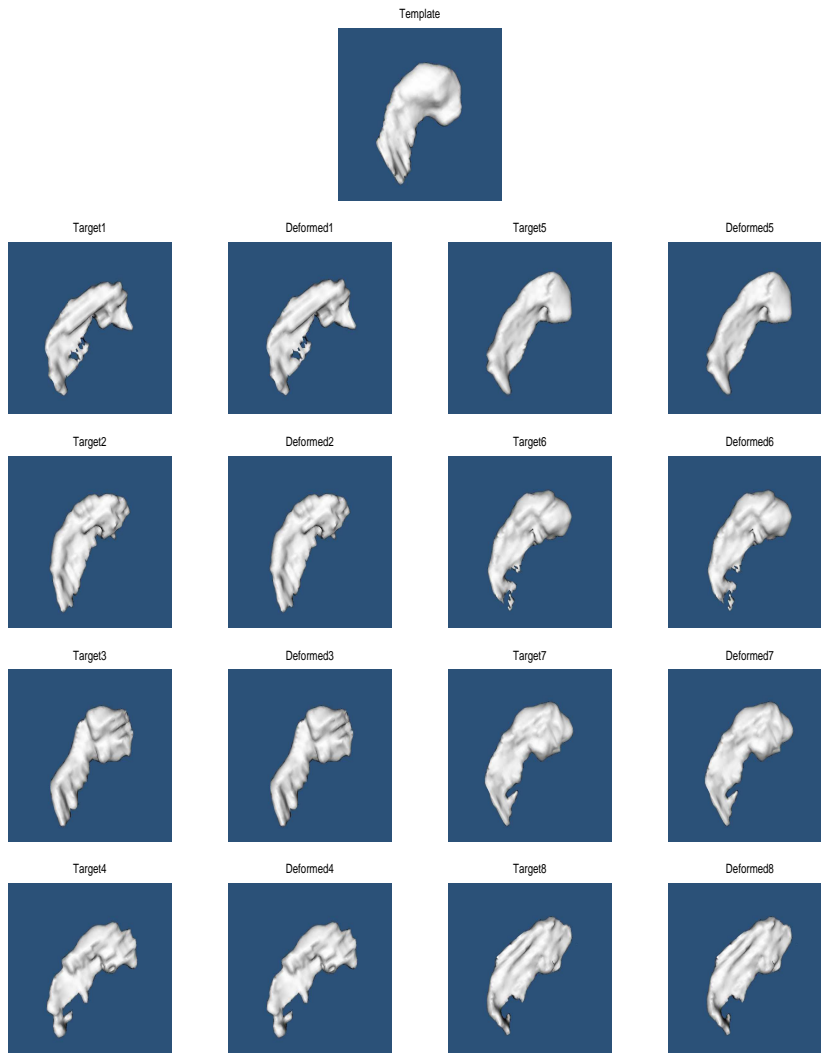


Fig. 5.10: Registration of the right hippocampus as described in Example 7. The template is in the first row, the eight right hippocampus target images are in the first and third columns, and corresponding eight deformed images are in the second and fourth columns.

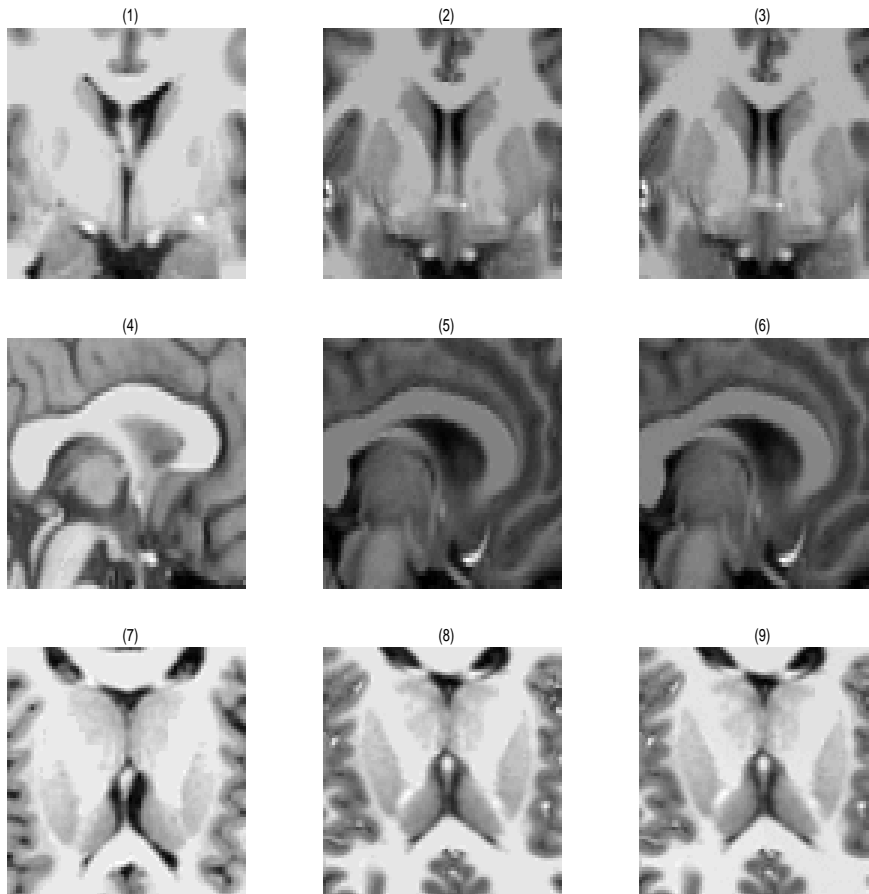


Fig. 5.11: Example 8. Registration of gray-scale 2D slices taken from 3D brain MR images. Shown are (1), (2) and (3) the midcoronal slices, (4), (5) and (6) the mid-sagittal slices and (7), (8) and (9) the midhorizontal slices. The template image, the target image, and the deformed template image are shown in the first, second, and third columns, respectively.

5.2. Summary of Results. The computational speed of the FDMKP and PMAE methods depends upon the size of the images and the respective number of iterations required to obtain a good approximation, but for our implementations the PMAE approach is always considerably faster. In what follows, all stated run times are for the PMAE, and all computer experiments are run in Fortran on a laptop with a single 1GHz processor and 1Gb of memory. For 2D images of size 32×32 , it takes only 5 to 10 seconds to obtain a very good approximate solution. For 2D images of size 80×80 , it takes from 1 to 3 minutes, and for 3D images of size $128 \times 128 \times 128$, it takes 2 to 3 hours. Now that a proof of concept and several benchmarks have been established several promising methods for speeding this up are currently being investigated. Table 5.1 shows average run times and results for a typical 3D dataset.

Many metric measures for determining the accuracy of numerical registration have been proposed in the literature, and we consider five of them here in order to compare the results of others. The overlay error is defined as

$$E_{\text{overlay}} = \frac{1}{|\Omega|} \|\rho_0 \circ \phi^{-1} - \rho_1\|_{L^1}, \quad (5.2)$$

where $\|f\|_{L^1} = \int_{\Omega} |f(x)| dx$, $|\Omega|$ is the area or volume of Ω (in 2D or 3D, respectively), and $\rho \circ \phi^{-1}$ is the deformed template image. The relative error defined as

$$E_{\text{relative}} = \|\rho_0 \circ \phi^{-1} - \rho_1\|_{L^2} / \|\rho_0 - \rho_1\|_{L^2}. \quad (5.3)$$

In Table 5.2 we show the relative error, the overlay error, and the L^2 -Kantorovich distance for some sample anatomical datasets.

To examine the quality of the registration images, we also use a similarity measure defined as follows. We first compute the optimal mapping that registers an MRI template image to an MRI target image. We then use it to map a given manually segmented template, to generate a segmented image — this is referred to as an automated segmentation. In Figure 5.12 and Figure 5.13 we show coronal slices of the manual and automated segmentations outlines overlaid on top of the gray-scale image for left and right hippocampus respectively.

To assess the performance of the MKP methods for image registration, we use manually segmented regions in both the template and the target images which can be found in the Internet Brain Segmentation Repository (IBSR). IBRS is an open online database with 18 MR brain 3D images and their associated segmentations¹. To evaluate the accuracy of our registration methods we compute the Kappa overlap metric between the regions segmented using our algorithm and that of the IBRS. The Kappa overlap metric (κ -metric) [?] is a similarity measure defined as

$$\kappa(\mathbf{I}, \mathbf{J}) = \frac{2n(\mathbf{I} \cap \mathbf{J})}{n(\mathbf{I}) + n(\mathbf{J})}, \quad (5.4)$$

where $n(A)$ is the number of voxels in image A . The overlap metric measures the similarity of two sets and ranges from 0 for sets that are disjoint and 1 for sets that are identical. The Kappa values of 0.7 or higher are considered as an excellent agreement (cf. [?]). In Tables 5.3 and 5.4 we show the measurements of the Kappa metric of manual and automated segmentations for some given 3D datasets for some MRI left hippocampus of size $42 \times 64 \times 64$ and some MRI right hippocampus of size

¹<http://www.cma.mgh.harvard.edu/ibsr/>

$44 \times 80 \times 64$ experiments. The average kappa value is 0.75 with standard deviation 0.037 for the left hippocampus and is 0.77 with standard deviation 0.035 for the right hippocampus. The accuracy is comparable to the results reported in [?, ?, ?], for example in [?] the average kappa value is 0.71 with standard deviation 0.057.

The Kappa overlap metric (5.4) is sensitive to both differences in location and size. Therefore we use the volume error, defined for two images I and J with volumes V_I and V_J as

$$E_{\text{volume}} = \frac{|V_I - V_J|}{V_I}, \quad (5.5)$$

to measure the difference in size. In Tables 5.3 and 5.4 we show the volume error for 3D datasets for the left and right hippocampus experiments.

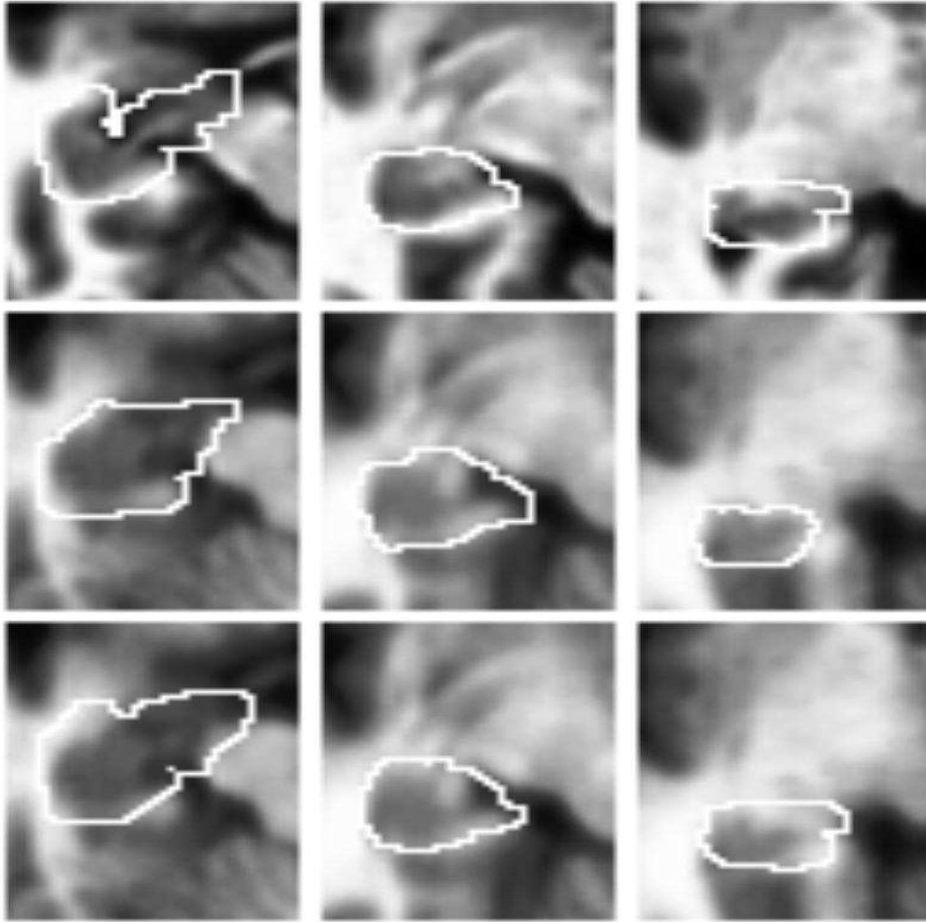


Fig. 5.12: Three coronal slices of left hippocampus: Segmentation outlines overlaid on top of the gray-scale image. First row is the template manual segmentations. Second row is the target manual segmentations. The third row is automated segmentations.

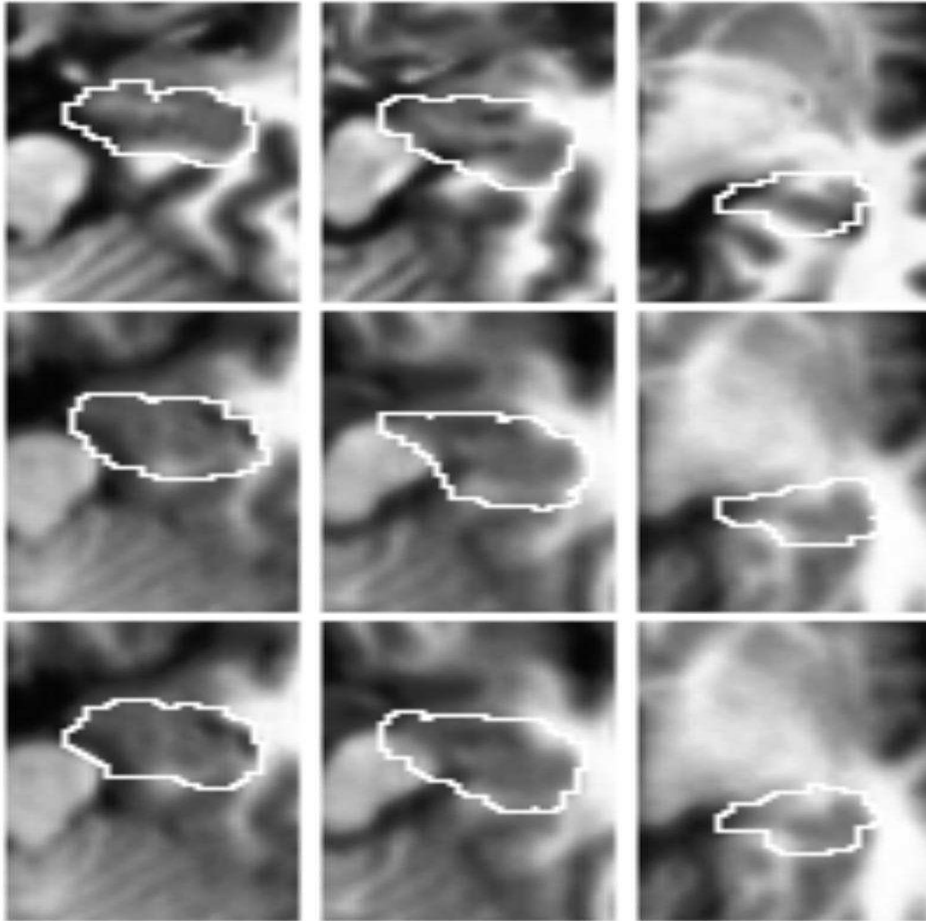


Fig. 5.13: Three coronal slices of right hippocampus: Segmentation outlines overlaid on top of the gray-scale image. First row is the template manual segmentations. Second row is the target manual segmentations. The third row is automated segmentations.

Dataset	Size of dataset	Run time in minutes
Hippocampus	$40 \times 64 \times 64$	14.58
Brain MRI	$80 \times 56 \times 80$	31.75
Heart	$128 \times 128 \times 128$	126.73

Table 5.1: Typical average run-time results for some 3D data sets for PMAE.

6. Discussion. We have presented two approaches based on solving the MAE (2.9) for elastic registration. From the known theory for the Monge-Kantorovich problem, existence and uniqueness of the optimal matching mapping are guaranteed, helping to assure that our methods are both robust and reliable.

The FDMKP method for image registration problems, introduced in Section 4,

Dataset	Overlay Error	Relative error	L^2 -Kantorovich distance
two concentric circles	0.0010	0.24 %	0.0305
circle to C-shape	0.0003	0.06 %	0.0341
macaque	1.0355e-10	2.5774e-06%	0.0100
left hippocampus	0.0008 \pm 0.0005	1.37 % \pm 0.80%	0.0018 \pm 0.0003
right hippocampus	0.0010 \pm 0.0006	1.77 % \pm 0.95%	0.0020 \pm 0.0003
heart	0.0060 \pm 0.0018	5.46% \pm 1.23%	0.0193 \pm 0.0041
brain (MRI)	0.0113	7.11 %	0.0088

Table 5.2: Overlay error, relative error, and L^2 -Kantorovich distance for some sample 3D datasets.

Dataset	Kappa	Volume Error	Dataset	Kappa	Volume Error
IBSR ₀₁ /ir	0.76	0.10	IBSR ₁₁ /ir	0.81	0.11
IBSR ₀₂ /ir	0.75	0.02	IBSR ₁₂ /ir	0.78	0.07
IBSR ₀₃ /ir	0.68	0.03	IBSR ₁₃ /ir	0.78	0.24
IBSR ₀₄ /ir	0.81	0.04	IBSR ₁₄ /ir	0.79	0.3
IBSR ₀₅ /ir	0.75	0.01	IBSR ₁₅ /ir	0.77	0.3
IBSR ₀₆ /ir	0.76	0.25	IBSR ₁₆ /ir	0.69	0.51
IBSR ₀₇ /ir	0.76	0.05	IBSR ₁₇ /ir	0.77	0.30
IBSR ₀₈ /ir	0.72	0.48	IBSR ₁₈ /ir	0.70	0.45
IBSR ₁₀ /ir	0.75	0.35			

Table 5.3: Left hippocampus: Kappa overlap metric and volume error. The mean value for Kappa overlap is 0.75523 with standard deviation 0.037459. The mean value for volume error is 0.21362 with standard deviation 0.17166

works well for 2D problems. However, for 3D the ALG2 algorithm introduced to solve the saddle point problem for the FDMKP method involves solving a 4-dimensional Poisson equation which introduces substantial computational difficulties. In contrast, we have successfully implemented the PMAE method for both 2D and 3D registration problems. Our approach for solving the PMAE (3.1) bears a close relationship to that of [?], for which a gradient descent method is introduced to solve for the optimal mapping. However, the method in [?] requires finding an initial mapping satisfying (2.3) and solving a Poisson equation at each step time, which would make the method very computationally expensive for large 3D registration problems. In contrast, our PMAE approach requires no construction of an initial mapping (always using a uniform initial mesh) and does not involve solving a Poisson equation at each stage.

The PMAE method has been tested for binary images as well as for gray scale images for 3D registration problems and found to give good results. We conclude that it shows considerable promise for general image registration problems when the region to be registered is away from the boundary. In the future, we intend to investigate other techniques for solving the original Monge-Ampère equation (2.9) and in optimizing the user specified parameters in order to develop the most suitable implementations for real world medical applications.

dataset	Kappa	Volume Error	dataset	Kappa	Volume Error
IBSR ₀₁ /ir	0.80	0.07	IBSR ₁₁ /ir	0.79	0.04
IBSR ₀₂ /ir	0.79	0.08	IBSR ₁₂ /ir	0.78	0.05
IBSR ₀₃ /ir	0.73	0.09	IBSR ₁₃ /ir	0.80	0.14
IBSR ₀₄ /ir	0.80	0.09	IBSR ₁₄ /ir	0.81	0.17
IBSR ₀₅ /ir	0.77	0.08	IBSR ₁₅ /ir	0.77	0.29
IBSR ₀₆ /ir	0.81	0.17	IBSR ₁₆ /ir	0.69	0.46
IBSR ₀₇ /ir	0.81	0.12	IBSR ₁₇ /ir	0.76	0.27
IBSR ₀₈ /ir	0.71	0.49	IBSR ₁₈ /ir	0.76	0.36
IBSR ₁₀ /ir	0.76	0.33			

Table 5.4: Right Hippocampus: Shown here are Kappa overlap metric and the volume error. The mean value for Kappa overlap is 0.77311 with standard deviation 0.035865. The mean value for the volume error is 0.19449 with standard deviation 0.14413.

7. Acknowledgements. The authors wish to thank the anonymous referees whose suggestions greatly improved this paper.

REFERENCES

- [1] L. AMBROSIO, *Lecture notes on optimal transport problems*, in Mathematical aspects of evolving interfaces (Funchal, 2000), vol. 1812 of Lecture Notes in Math., Springer, Berlin, 2003, pp. 1–52.
- [2] L. AMBROSIO, L. A. CAFFARELLI, Y. BRENIER, G. BUTTAZZO, AND C. VILLANI, *Optimal transportation and applications*, vol. 1813 of Lecture Notes in Mathematics, Springer-Verlag, Berlin, 2003. Lectures from the C.I.M.E. Summer School held in Martina Franca, September 2–8, 2001, Edited by Caffarelli and S. Salsa.
- [3] S. ANGENENT, S. HAKER, AND A. TANNENBAUM, *Minimizing flows for the Monge-Kantorovich problem*, SIAM J. Math. Anal., 35 (2003), pp. 61–97 (electronic).
- [4] M. F. BEG, M. MILLER, A. TROUVE, AND L. YOUNES, *The euler-lagrange equation for interpolating sequence of landmark datasets*, Medical Image Computing and Computer-Assisted Intervention - Miccai 2003, Pt 2, 2879 (2003), pp. 918–925.
- [5] M. F. BEG, M. I. MILLER, A. TROUVÉ, AND L. YOUNES, *Computing large deformation metric mappings via geodesic flows of diffeomorphisms*, Int. J. Comput. Vision, 61 (2005), pp. 139–157.
- [6] J.-D. BENAMOU AND Y. BRENIER, *A computational fluid mechanics solution to the Monge-Kantorovich mass transfer problem*, Numer. Math., 84 (2000), pp. 375–393.
- [7] J. D. BENAMOU AND Y. BRENIER, *Mixed L^2 -Wasserstein optimal mapping between prescribed density functions*, J. Optim. Theory Appl., 111 (2001), pp. 255–271.
- [8] F. L. BOOKSTEIN, *Principal warps - thin-plate splines and the decomposition of deformations*, Ieee Transactions on Pattern Analysis and Machine Intelligence, 11 (1989), pp. 567–585.
- [9] Y. BRENIER, *Polar factorization and monotone rearrangement of vector-valued functions*, Comm. Pure Appl. Math., 44 (1991), pp. 375–417.
- [10] C. J. BUDD AND J. F. WILLIAMS, *Parabolic Monge-Ampère methods for blow-up problems in several spatial dimensions*, J. Phys. A, 39 (2006), pp. 5425–5444.
- [11] ———, *Moving mesh generation using the parabolic Monge-Ampère equation*, In press, SIAM J. Sci. Comp., (2008).
- [12] L. A. CAFFARELLI, *Boundary regularity of maps with convex potentials*, Comm. Pure Appl. Math., 45 (1992), pp. 1141–1151.
- [13] ———, *The regularity of mappings with a convex potential*, J. Amer. Math. Soc., 5 (1992), pp. 99–104.
- [14] G. E. CHRISTENSEN, S. C. JOSHI, AND M. I. MILLER, *Volumetric transformation of brain anatomy*, Ieee Transactions on Medical Imaging, 16 (1997), pp. 864–877.
- [15] H. CHUI, J. RAMBO, J. DUNCAN, R. SCHULTZ, AND A. RANGARAJAN, *Registration of cortical anatomical structures via robust 3d point matching*, Information Processing in Medical

- Imaging, Proceedings, 1613 (1999), pp. 168–181.
- [16] D. L. COLLINS, P. NEELIN, T. M. PETERS, AND A. C. EVANS, *Automatic 3d intersubject registration of mr volumetric data in standardized talairach space*, Journal of Computer Assisted Tomography, 18 (1994), pp. 192–205.
- [17] E. R. E. DENTON, L. I. SONODA, D. RUECKERT, S. C. RANKIN, C. HAYES, M. O. LEACH, D. L. G. HILL, AND D. J. HAWKES, *Comparison and evaluation of rigid, affine, and nonrigid registration of breast mr images*, Journal of Computer Assisted Tomography, 23 (1999), pp. 800–805.
- [18] L. C. EVANS AND W. GANGBO, *Differential equations methods for the Monge-Kantorovich mass transfer problem*, Mem. Amer. Math. Soc., 137 (1999), pp. viii+66.
- [19] J. C. GEE, D. R. HAYNOR, L. LEBRIQUER, AND R. K. BAJCSY, *Advances in elastic matching theory and its implementation*, Cvrmed-Mrcas’97, 1205 (1997), pp. 63–72.
- [20] J. C. GEE, M. REIVICH, AND R. BAJCSY, *Elastically deforming 3d atlas to match anatomical brain images*, Journal of Computer Assisted Tomography, 17 (1993), pp. 225–236.
- [21] A. GHOLIPOUR, N. KEHTARNAVAZ, R. BRIGGS, M. DEVOUS, AND K. GOPINATH, *Brain functional localization: A survey of image registration techniques*, Ieee Transactions on Medical Imaging, 26 (2007), pp. 427–451.
- [22] S. HAKER AND A. TANNENBAUM, *Optimal mass transport and image registration*, Variational and Level Set Methods in Computer Vision, 2001. Proceedings. IEEE Workshop on, (2001), pp. 29–36.
- [23] S. HAKER AND A. TANNENBAUM, *On the Monge-Kantorovich problem and image warping*, in Mathematical methods in computer vision, vol. 133 of IMA Vol. Math. Appl., Springer, New York, 2003, pp. 65–85.
- [24] S. HAKER, L. ZHU, A. TANNENBAUM, AND S. ANGENENT, *Optimal mass transport for registration and warping*, Internat. J. Computer Vision, 60 (2004), pp. 225–240.
- [25] D. L. G. HILL, P. G. BATCHELOR, M. HOLDEN, AND D. J. HAWKES, *Medical image registration*, Physics in Medicine and Biology, 46 (2001), pp. R1–R45.
- [26] W. HINTERBERGER AND O. SCHERZER, *Models for image interpolation based on the optical flow*, Computing, 66 (2001), pp. 231–247.
- [27] M. HOLDEN, D. L. G. HILL, E. R. E. DENTON, J. M. JAROSZ, T. C. S. COX, AND D. J. HAWKES, *Voxel similarity measures for 3d serial mr brain image registration*, Information Processing in Medical Imaging, Proceedings, 1613 (1999), pp. 472–477.
- [28] A. JOSHI, D. SHATTUCK, P. THOMPSON, AND R. LEAHY, *Surface-constrained volumetric brain registration using harmonic mappings*, Medical Imaging, IEEE Transactions on, 26 (2007), pp. 1657–1669.
- [29] A. A. JOSHI, D. W. SHATTUCK, P. M. THOMPSON, AND R. M. LEAHY, *A framework for registration, statistical characterization and classification of cortically constrained functional imaging data*, Information Processing in Medical Imaging, Proceedings, 3565 (2005), pp. 186–196.
- [30] S. C. JOSHI AND M. I. MILLER, *Landmark matching via large deformation diffeomorphisms*, Ieee Transactions on Image Processing, 9 (2000), pp. 1357–1370.
- [31] A. KHAN, L. WANG, AND M. F. BEG, *Freesurfer-initiated fully-automated sub-cortical brain segmentation in mri using large deformation diffeomorphic metric mapping*, NeuroImage (accepted), (2008).
- [32] M. KNOTT AND C. S. SMITH, *On the optimal mapping of distributions*, J. Optim. Theory Appl., 43 (1984), pp. 39–49.
- [33] A. LEOW, S. C. HUANG, A. GENG, J. BECKER, S. DAVIS, A. TOGA, AND P. THOMPSON, *Inverse consistent mapping in 3d deformable image registration: Its construction and statistical properties*, Information Processing in Medical Imaging, Proceedings, 3565 (2005), pp. 493–503.
- [34] J. LIU, D. CHELBERG, C. SMITH, AND H. CHEBROLU, *Automatic subcortical structure segmentation using probabilistic atlas*, Advances in Visual Computing, (2007), pp. 170–178.
- [35] A. PITIOT, E. BARDINET, P. M. THOMPSON, AND G. MALANDAIN, *Piecewise affine registration of biological images for volume reconstruction*, Medical Image Analysis, 10 (2006), pp. 465–483.
- [36] J. P. W. PLUIM, J. B. A. MAINTZ, AND M. A. VIERGEVER, *Mutual-information-based registration of medical images: A survey*, Ieee Transactions on Medical Imaging, 22 (2003), pp. 986–1004.
- [37] D. RUECKERT, L. I. SONODA, C. HAYES, D. L. G. HILL, M. O. LEACH, AND D. J. HAWKES, *Nonrigid registration using free-form deformations: Application to breast mr images*, Ieee Transactions on Medical Imaging, 18 (1999), pp. 712–721.
- [38] M. J. SEWELL, *Maximum and minimum principles: A unified approach, with applications*,

- Cambridge Texts in Applied Mathematics, Cambridge University Press, Cambridge, 1987.
- [39] D. G. SHEN AND C. DAVATZIKOS, *Hammer: Hierarchical attribute matching mechanism for elastic registration*, Ieee Transactions on Medical Imaging, 21 (2002), pp. 1421–1439.
 - [40] ———, *Very high-resolution morphometry using mass-preserving deformations and hammer elastic registration*, Neuroimage, 18 (2003), pp. 28–41.
 - [41] C. STUDHOLME, J. A. LITTLE, G. P. PENNY, D. L. G. HILL, AND D. J. HAWKES, *Automated multimodality registration using the full affine transformation: Application to mr and ct guided skull base surgery*, Visualization in Biomedical Computing, 1131 (1996), pp. 601–606.
 - [42] M. H. M. SULMAN, *Optimal Mass Transport for Adaptivity and Image Registration*, PhD thesis, Simon Fraser University, August 2008.
 - [43] J. P. THIRION, *New feature points based on geometric invariants for 3d image registration*, International Journal of Computer Vision, 18 (1996), pp. 121–137.
 - [44] A. W. TOGA AND P. M. THOMPSON, *The role of image registration in brain mapping*, Image and Vision Computing, 19 (2001), pp. 3–24.
 - [45] M. VAILLANT AND J. GLAUNES, *Surface matching via currents*, Information Processing in Medical Imaging, Proceedings, 3565 (2005), pp. 381–392.
 - [46] C. VILLANI, *Topics in optimal transportation*, vol. 58 of Graduate Studies in Mathematics, American Mathematical Society, Providence, RI, 2003.
 - [47] A. P. ZIJDENBOS, R. A. DAWANT, AND A. C. PALMER, *Morphometric analysis of white matter lesions in mr images: method and validation*, IEEE Trans. Med. Imaging, 13 (1994), pp. 716–724.

8. Appendix. All mappings presented in this paper were computed using one of the two following algorithms. Given two images ρ_0 and ρ_1 , then the simplest algorithm to compute the deformed template image is the following:

1- Using the PMAE method:

1. Normalize ρ_0 and ρ_1 so that they have the same mass, i.e.,

$$\rho_k = \rho_k / \int_{\Omega} \rho_k(x) dx, \quad k = 0, 1.$$

2. If in some regions the images have zero value then add small positive number ϵ , i.e.,

$$\rho_k = \epsilon + \rho_k, \quad k = 0, 1,$$

so that both are positive every where in the whole domain.

3. Use the PMAE method to compute the optimal mapping $\nabla\Psi$ that minimizes the functional (3.6).
4. Compute the deformed template

$$\rho_{\text{deform}} = \det(\nabla\Psi^{-1}) \rho_0 \circ \nabla\Psi^{-1} \tag{8.1}$$

The only two user adjustable parameters are the threshold ϵ and the stopping tolerance for the ODE solver. Typically $\epsilon = 1e-2$ and tolerance $\tau = 1e-4$. In our tests the results are not sensitive to the parameter tolerance τ once it is sufficiently small except to make the algorithm smaller. The platform ϵ affects not only the stiffness of the problem but also the possibility of artificially deforming regions of images. The optimal choice depends on several factors and we are currently investigating ways to choose it automatically.

2- Using the FDMKP method

1. Normalize ρ_0 and ρ_1 so that they have the same mass, i.e.,

$$\rho_k = \frac{\rho_k}{\int_{\Omega} \rho_k(x) dx}, \quad k = 0, 1.$$

2. If in some regions the images have zero value then add small positive number ϵ , i.e.,

$$\rho_k = \epsilon + \rho_k, \quad k = 0, 1,$$

so that both are positive every where in the whole domain.

3. Use the FDMKP method to compute the optimal velocity and density fields $v(x, t)$ and $\rho(x, t)$, for $x \in \Omega$, $0 \leq t \leq 1$, that minimize the energy functional (4.3).
4. The deformed template is

$$\rho_{\text{deform}} = \rho(\cdot, 1)$$

Solution of the saddle point problem associated to the FDMKP requires that the user specify two parameters. In our experience, the code performs well for a wide range of parameters.